Nuclear Science and Techniques (2024) 35:188
https://doi.org/10.1007/s41365-024-01530-1

Simulation and experimental comparison of the performance of four-corner-readout plastic scintillator muon-detector system

Lie He[1,2] · Si-Yuan Luo[1,2] · Xiang-Man Liu[3,4,5] · Yu-Cheng Zou[1,2] · Hai-Feng Zhang[1,2] · Wan-Cheng Xiao[1,2] · Yu-He Huang[6] · Xiao-Dong Wang[1,2]

Received: 4 November 2023 / Revised: 7 March 2024 / Accepted: 20 March 2024 / Published online: 9 October 2024

Abstract

Cosmic-ray muons are highly penetrating background-radiation particles found in natural environments. In this study, we develop and test a plastic scintillator muon detector based on machine-learning algorithms. The detector underwent muon position-resolution tests at the Institute of Modern Physics in Lanzhou using a multiwire drift chamber (MWDC) experimental platform. In the simulation, the same structural and performance parameters were maintained to ensure the reliability of the simulation results. The Gaussian process regression (GPR) algorithm was used as the position-reconstruction algorithm owing to its optimal performance. The results of the Time Difference of Arrival algorithm were incorporated as one of the features of the GPR model to reconstruct the muon hit positions. The accuracy of the position reconstruction was evaluated by comparing the experimental results with Geant4 simulation results. In the simulation, large-area plastic scintillator detectors achieved a position resolution better than 20 mm. In the experimental-platform tests, the position resolutions of the test detectors were 27.9 mm. We also analyzed factors affecting the position resolution, including the critical angle of the total internal reflection of the photomultiplier tubes and distribution of muons in the MWDC. Simulations were performed to image both large objects and objects with different atomic numbers. The results showed that the system could image high- and low-Z materials in the constructed model and distinguish objects with significant density differences. This study demonstrates the feasibility of the proposed system, thereby providing a new detector system for muon-imaging applications.

Keywords Monte Carlo simulation · Muon tomography · TDOA · Machine learning · Image reconstruction

1 Introduction

Muons are fundamental particles with a spin of 1/2 and a mass that is approximately 207 times that of an electron. When cosmic-ray particles collide with atmospheric molecules, they produce a large number of secondary particles, including pions (π mesons) and kaons (K mesons). These mesons decay into muons over a short period, which

This work was supported by the National Natural Science Foundation of China (Nos. 12275120, 11875163), Ministry of Science and Technology of China (No. 2020YFE0202001), Science and Technology Innovation Program of Hunan Province (No. 2022RC1202), and Hunan Provincial Natural Science Foundation (No. 2021JJ20006).

✉ Xiao-Dong Wang
wangxd@usc.edu.cn

1 School of Nuclear Science and Technology, University of South China, Hengyang 421001, China

2 Key Laboratory of Advanced Nuclear Energy Design and Safety (MOE), University of South China, Hengyang 421001, China

3 Institute of Modern Physics, Chinese Academy of Sciences, Lanzhou 730000, China

4 School of Nuclear Science and Technology, University of Chinese Academy of Sciences, Beijing 100049, China

5 School of Nuclear Science and Technology, Lanzhou University, Lanzhou 730000, China

6 School of Physical Sciences, University of Science and Technology of China, Hefei 230026, China

continue to propagate and reach the Earth's surface [1, 2]. At sea level, muons exhibit a continuous energy spectrum with an average energy of approximately 3–4 GeV. They possess an extremely high penetrating power, enabling them to pass through the Earth's atmosphere and penetrate several kilometers into the Earth's crust [3, 4]. Based on this property, muon imaging has been applied in geological exploration and other applications [5, 6]. In recent years, research on the use of muons for noninvasive imaging applications has expanded [7], and muon-imaging techniques can be classified into muon transmission, muon multiple scattering, and muon and its secondary particle imaging. Transmission imaging is based on the flux change of the muons after they pass through a material. Alvarez first used this technique in 1970 to discover new chambers inside a pyramid [8]. Subsequently, this method has been widely applied to volcano studies [9], underground tunneling [10], hydrogeological research [11], and the exploration of unknown structures within the Cheops Pyramid [12]. Multiple-scattering tomography, which calculates the variation in the scattering angle in the same muon trajectory to infer the atomic composition, was first proposed and used by the Los Alamos National Laboratory in the USA to identify high-Z materials in a short time [13]. Subsequently, muon tomography was applied in areas such as customs container inspection [14], nuclear-material monitoring [15], and spent-fuel regulatory management [16]. The imaging of muons and their secondary particles involves utilizing information carried by neutrons, electrons, and gamma rays generated through the interaction of muons with matter. Mrdja et al. proposed a new imaging method that used muons and their secondary particles [17, 18]. Muon imaging of low-Z materials was achieved for the first time by experimentally reconstructing a three-dimensional image of a bovine femur. A related study was also conducted by a research team at the University of South China [19, 20]; they theoretically proposed a new method of 4D imaging using a conformal detection technique for cosmic-ray muons and their secondary particles. However, muon-imaging technology faces several challenges in practical applications. For example, achieving a larger detection area and faster track positioning is difficult while maintaining good resolution accuracy.

Machine learning has been increasingly applied in the field of muon imaging as a novel approach [21, 22]. In particular, for the application of muon hit-position estimation [23], this method involves training on a large-scale database to learn the response characteristics of detectors and transmission rules of muons within detectors [24]. Compared to traditional methods, machine learning can achieve a higher reconstruction accuracy, making it a promising technology with significant potential in the field of muon imaging.

Currently, detectors capable of muon-track localization face certain issues and inconveniences. Common muon detectors include scintillator strip detectors with wavelength-shifting (WLS) fibers [25], micropattern gas detectors [26–28] (such as micromegas detectors, gas electron multiplier detectors, and multiwire drift chambers (MWDCs), etc.), and nuclear-emulsion detectors [29]. Among these three types, gas detectors have relatively complex structures, leading to high manufacturing costs and stringent process requirements. The imaging method for nuclear-emulsion detectors provides no timing information and requires the replacement of the emulsion films after each use. The scintillator strip detector uses WLS fibers to guide the scintillation photons generated by the corresponding position of the scintillator strip to the photodetector devices for detecting and recording the position of the muons. Scintillator strips can be classified into rectangular and triangular strips, and the precision of the detector is limited by the number and size of the scintillator strips. To achieve high precision, this system requires a large number of scintillator strips, a corresponding number of photodetector devices, and a high level of craftsmanship to ensure perfect coupling with the WLS fibers. Consequently, the cost of the system is high, and the calibration process is time consuming. These limitations restrict the practical application of existing muon detectors, and several research teams in China are currently conducting further studies to address this issue [30–32]. For example, a team at the Institute of Modern Physics, Lanzhou, used a multiwire proportional chamber to verify a new TOF detector scheme that couples undivided large-area plastic scintillators with photomultiplier tubes (PMTs). They achieved a positional resolution of 48 mm [33].

In this study, we propose a novel design for a muon-detection system. It utilizes a nonsegmented large-area plastic scintillator directly coupled to fast PMTs at the four corners of the scintillator panel. The muon hit positions are reconstructed using a combination of machine-learning algorithms and Time Difference of Arrival (TDOA) algorithms. This approach simplifies the device stacking on the detector panel, has a large detection area, is capable of covering more than one square meter in future developments, and requires only a small number of electronic circuits, resulting in cost reduction. Furthermore, this system offers the advantages of a simple and easy-to-build structure, minimal electronic components, and convenient portability. Based on the analysis of the results, this system achieves the reconstruction of the muon hit points and trajectories. In addition, by utilizing scattering-tomography techniques, the system achieves the image reconstruction of different density models.

2 Detector system configuration

2.1 Simulation parameters of detector system

2.1.1 Detector geometry design

Three components were simulated based on GEANT4.10.6p-03 software, as shown in Fig. 1. Figure 1a shows the structural model of a single detector. The material structure of an EJ-200 plastic scintillator was used as a reference. The dimensions of the model were set to 800 mm × 800 mm × 50 mm, and the material was filled with molecules with a chemical formula of C_9H_{10}, density of 1.023 g/cm^3, scintillation light yield of 10,000 photons/MeV, and peak emission wavelength of 425 nm. Based on the emission spectrum of EJ-200 [34] and the relationship between the reflectivity of the reflector layer and collection efficiency, a reflector layer with a reflectivity of 0.88 was placed on the surface of the plastic scintillator. Assuming a wavelength of 425 nm for the scintillation photons in the EJ-200 plastic scintillator, the estimated velocity (v) was approximately 0.633c. PMTs were constructed at the four corners of the detector field for response simulation. The effective diameter of the photocathode was set as 46 mm. As shown in Fig. 1b, two sets of track-detector modules were positioned separately at the top and bottom of the object under investigation. This arrangement enabled muon-scattering imaging based on the varying scattering angles of the tracks.

2.1.2 Basic performance simulation

The incident particle source was generated using an independent particle-source library (CRY) [35]. Owing to the inherent incident angles of natural muons, to determine the muon trajectory, an incident muon was recorded, and the data of the response photons collected by PMTs were analyzed only when a signal response was observed from both layers of detectors.

The dimensions and optical parameters of the detector model components considered in the simulation were as follows. EJ-200 had a refractive index of 1.58. Based on the relationship between reflectance and efficiency shown in Fig. 1a, the reflective foil was modeled as an additional volume located 0.1 mm away from the scintillator surface to enhance the light collection on the PMT photocathode. To simulate the actual conditions of the PMT window, as shown in Fig. 1c, a thin volume (0.2 mm thick) of the optical-coupling material is defined with silicon grease with a refractive index of 1.47. The area conversion from the square scintillator-end face (area $S_1 = 25$ cm^2) to the PMT sensitive-area surface (area $S_2 = 21.16$ cm^2) and the coupling effects between the scintillator and PMT must be considered. The

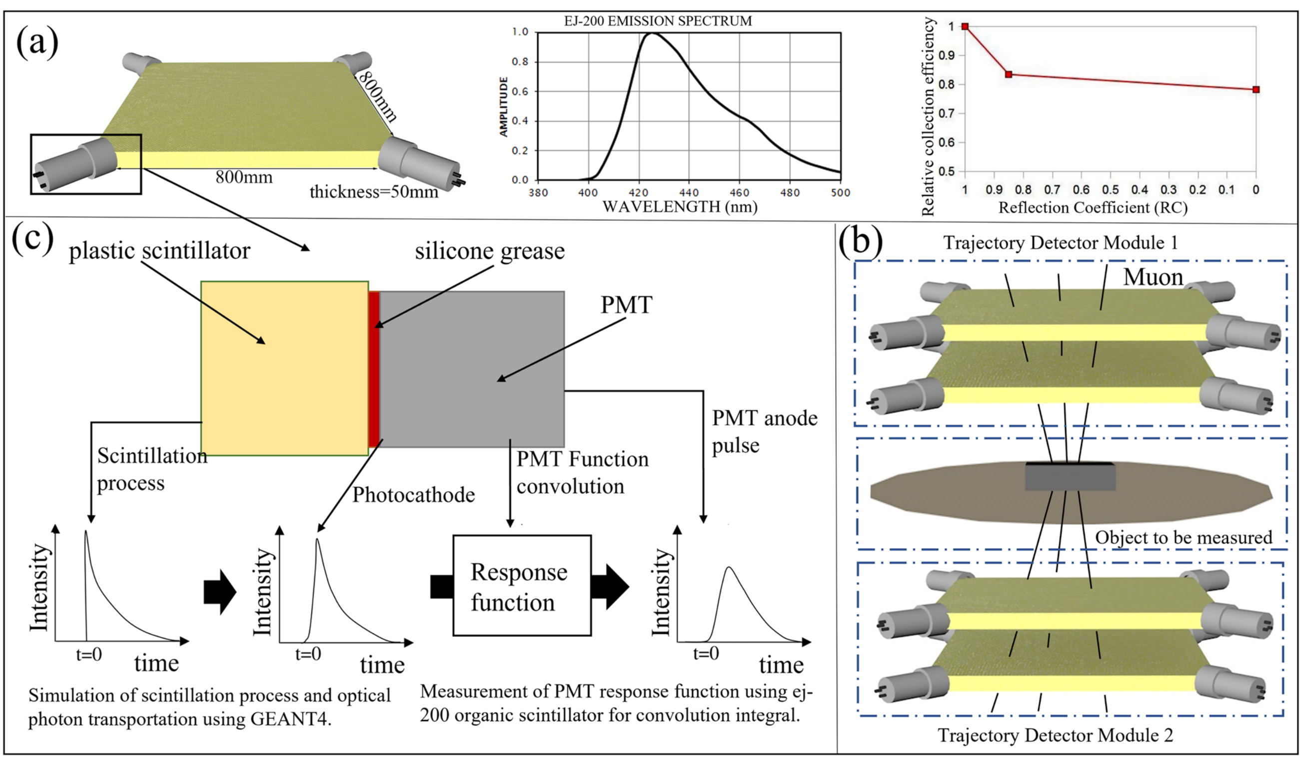

Fig. 1 (**a**) Single-layer detector and material parameters. (**b**) Muon-scattering imaging system. (**c**) Basic performance simulation

critical angle for the total internal reflection $\theta_c = \sin^{-1}\left(n_{grease}/n_{scint}\right)$ was calculated as 68.5°. The lower half of Fig. 1c illustrates the method based on the Geant4 simulation and PMT response-function measurements. This method involves recording the time at which each photon reaches the PMT, obtaining the distribution of photon-arrival times at the PMT photocathode, and using a photon response function to obtain simulated pulse signals [36]. When a single photoelectron arrives at the photocathode, the PMT generates a pulsed signal. The pulse waveform of a single photoelectron was simulated using the following time response function [37]: $v_i(t) = GC_e \frac{t^2 e^{-\frac{t^2}{\tau^2}}}{\int t^2 e^{-\frac{t^2}{\tau^2}} \mathrm{d}t}$, where G is the gain of the PMT, C_e represents the charge-to-voltage conversion factor, and τ represents the time constant of 2.5 ns, which is the rise time of the PMT detector. Because the arrival time of each photoelectron at the PMT is different, the simulated output signal of the PMT is obtained by summing the pulse waveforms of individual photoelectrons, as follows: $V_{PMT}(t) = \sum_{i=1}^{n} v_i(t)$.

2.2 Experimental platform and data acquisition

To ensure the validity and feasibility of the simulation results, we conducted position-resolution tests on the plastic-scintillator read out at the four corners using an MWDC experimental platform at the Institute of Modern Physics in Lanzhou, as shown in Fig. 2a. The testing platform comprised two layers, upper and lower multiwire drift chambers,

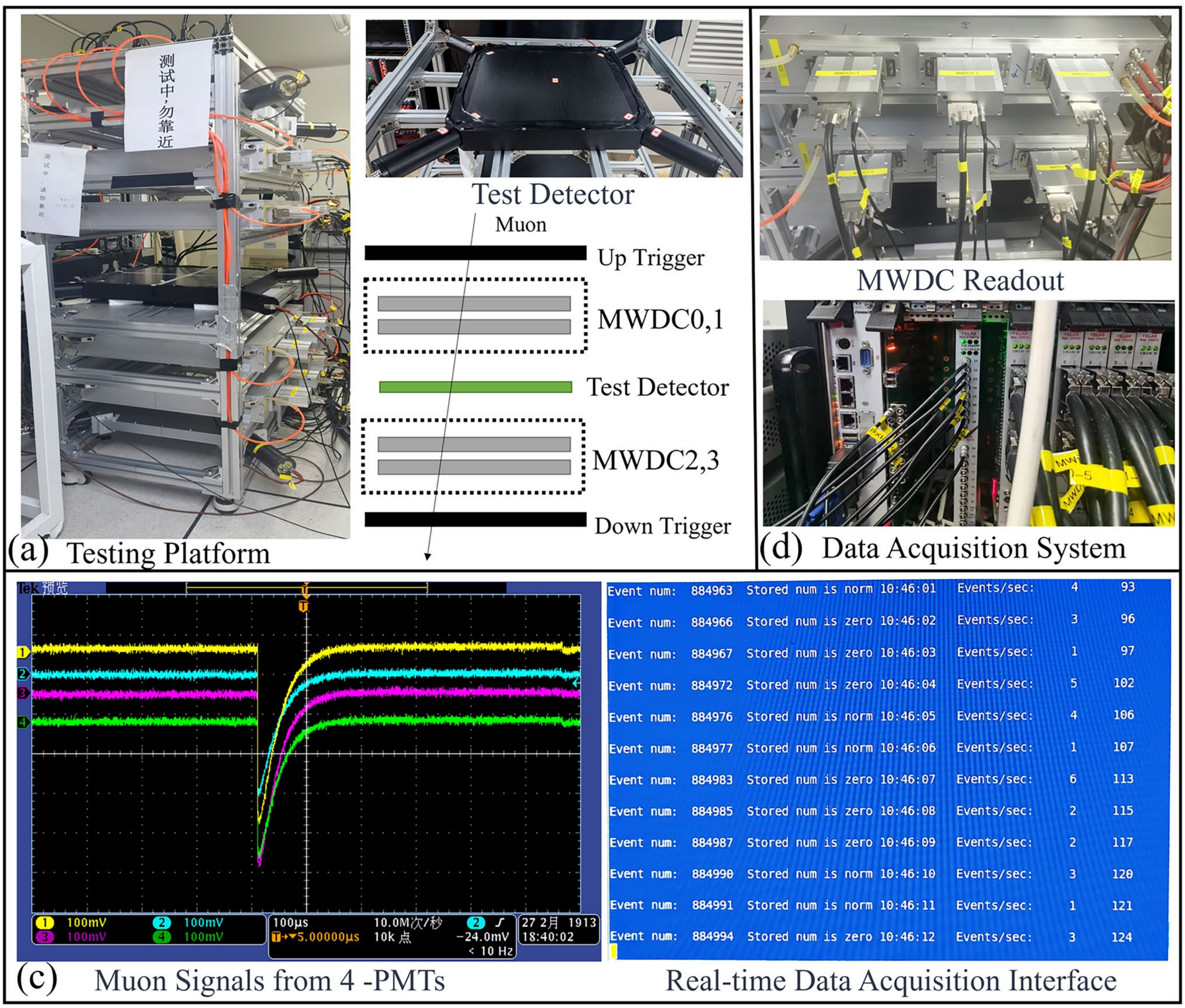

Fig. 2 (Color online) (**a**) Experimental testing platform. (**b**) Electronic data acquisition and readout. (**c**) Muon signal and real-time data-acquisition interface

which were used to determine the muon hit position and two plastic scintillator detectors for signal triggering. The tested plastic scintillator detector was placed in the middle of the two layers of detectors. Each MWDC had an effective area of 400 mm × 400 mm with four layers of anode wires to record the information and calculate the muon hit position. Because the position resolution of the MWDC was better than 300 μm [38], the muon hit position measured by the MWDC detector in the experiment was considered as the true muon incident position. The tested detector was placed in the middle of the platform, and the height of the detector above the ground was defined as the z-axis direction, which was approximately 48 cm. The principle of this experiment was to use the MWDC to measure the position resolution of the tested plastic scintillator detector. The system accepted and recorded a muon signal only when the trigger signals at the upper and lower ends simultaneously measured the signal within a specified time and responded. As shown in Fig. 2b, the backend electronic data-acquisition system recorded the data from the MWDC to determine the real hit positions of the muons and the muon signal obtained from the PMT, which are shown in the left panel of Fig. 2c. The data-acquisition system captures the trigger time and time over the threshold when the muon signal hits the plastic scintillator detector, enabling the subsequent implementation of machine-learning algorithms to reconstruct the muon hit position. Real-time signal-acquisition data for the muons are shown in the right panel of Fig. 2c. The acquisition interface displayed the number of muons collected per second as well as the total data volume and collection duration. Only when signals were input into the triggering detector, four-layer MWDC detector, and test detector simultaneously were they recorded as the final data. The average time resolution obtained from the four-corner readout experiment for the tested detector was approximately 312 ps, and this time resolution was used in Geant4 simulations as the readout response-time resolution.

2.3 Localization algorithms based on TDOA principle

This section proposes a spatial localization algorithm based on a hyperbolic curve model [39]. The algorithm uses the time differences of the photons reaching the four PMTs as information to reconstruct the position of the muon hitting the detector. Compared to traditional localization algorithms, the main advantage of this algorithm is that it only requires the time differences of photon arrivals at the four PMTs to reconstruct the hit position. This simplifies the detector structure, eliminating the need for additional trigger signals and "0" time provided by the detection system. (In traditional methods, the trigger time needs to be obtained through the triggering detector [33], and here, we define the starting time of the trigger as "0" time). The fundamental principle of this algorithm is that for any point on a hyperbola, the difference in the distance from that point to the two foci remains constant. For the detector, the positions of PMTs were set as the foci. When two sets of different hyperbolas intersect, their intersection points represent the impact position O of the muon, which is expressed as (X, Y). In the coordinate system, the PMT located at the common focus is considered the primary position (X_0, Y_0), whereas the positions of the other PMTs are denoted as (X_i, Y_i), where $i = 1, 2, 3, ..., n$. Using two hyperbolas (three PMTs), the detector can obtain the hit position in the plane coordinate system. The calculation process is as follows:

$$\begin{cases} R_0 = \sqrt{\left(x - x_0\right)^2 + \left(y - y_0\right)^2} \\ R_i = \sqrt{\left(x - x_i\right)^2 + \left(y - y_i\right)^2} \\ R_{i,0} = R_i - R_0 = v\left(t_i - t_0\right) \end{cases} \quad (1)$$

The hit position (X, Y, Z) can then be obtained from Eq. (1):

$$\begin{bmatrix} 2x_{1,0} & 2y_{1,0} & 2R_{1,0} \\ 2x_{2,0} & 2y_{2,0} & 2R_{2,0} \\ \cdots & \cdots & \cdots \\ 2x_{i,0} & 2y_{i,0} & 2R_{i,0} \end{bmatrix} \begin{bmatrix} x \\ y \\ R_0 \end{bmatrix} = \begin{bmatrix} K_1 - K_0 - R_{1,0}^2 \\ K_2 - K_0 - R_{2,0}^2 \\ \cdots \\ K_3 - K_0 - R_{i,0}^2 \end{bmatrix} \quad (2)$$

$$\mathbf{GZ} = \mathbf{P}. \quad (3)$$

In this equation, $K_i = x_i^2 + y_i^2$ (for $i = 0, 1, 2, 3$), where K_i denotes the square of the distance from each PMT to the coordinate origin. The distance between the incident point and ith PMT is represented by R_i. Solving for $\mathbf{Z}$ in Eq. (3) yields the impact position (x, y). Owing to potential timing errors in the detectors, the equation may have no solution. In such cases, an approximate solution for the impact position can be obtained through multiple iterations using the least-squares method.

2.4 Position reconstruction with machine-learning algorithms

2.4.1 Selection of machine-learning models

To further improve the accuracy of muon-hit-position reconstruction, machine-learning algorithms were introduced for optimization. Four commonly used machine-learning models were investigated: Gaussian process regression (GPR), support vector machines (SVMs), decision trees (DTs), and backpropagation (BP) neural networks. The position coordinates obtained from the localization algorithm described in the previous section were included as features in the feature dataset. The features in this dataset also included the peak and start times of the PMT responses obtained from the simulations. A flowchart of the machine-learning models is shown in Fig. 3a.

When training a model, data points that exhibit significant differences must be selected to improve the generalizability of the model. This prevents the training results from being biased towards frequently occurring data, thereby ensuring a balanced data distribution and preventing the model from becoming ineffective. However, it is crucial to guard against overfitting, which can result in a model that performs well on the training set but poorly on the test set. To mitigate this, a portion of the training data should be randomly reserved as a validation set. Using a validation set to tune the hyperparameters of the machine-learning model, we can avoid overfitting the training set and improve the model's generalizability. Box plots provide a visual representation of the dataset's central tendency, dispersion, and outliers, allowing the evaluation of the performance of the machine-learning algorithms. The box length in a box plot represents the dispersion of the data. The median position indicates the central tendency of the data, whereas the upper and lower quartiles (Q1 and Q3) represent the degree of data dispersion. Points outside the box, called outliers, represent data values outside the error range.

During the data-training process, the same algorithm was used to build models for the x- and y-axis coordinate data values separately [24], with the aim of improving the accuracy of the model predictions. As shown in Fig. 3b, the simulated muons hit the scintillator plate at the marked positions, and the PMT response data were obtained to create a feature dataset. These hit points were spaced 10 mm apart, and a total of 5776 known positional data points were used to train and validate the model. To mitigate the effects of randomness and augment the training dataset, we simulated each point five times, resulting in a total of 28880 datasets. The test dataset was independent of the training dataset. Following the muon-incidence pattern, the muons were

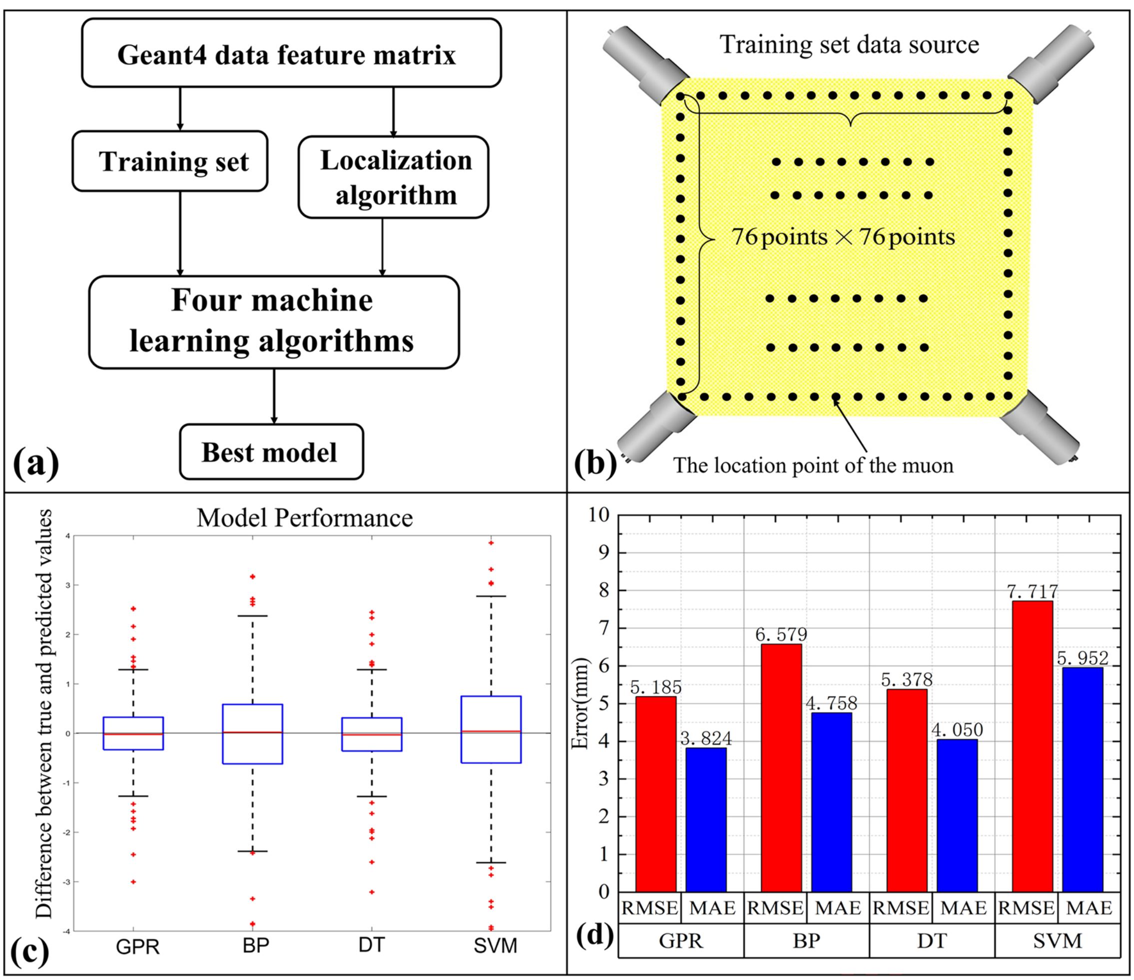

Fig. 3 (Color online) (**a**) Training process of the machine-learning models. (**b**) Selection of data points for the training sets. (**c**) Box plots showing the performance of the four machine-learning models. (**d**). Average error and residual plots of the validation set for four machine-learning models

randomly incident on the detector field, and the collected data were stored as the test set.

The performances of the four machine-learning models are shown in Fig. 3c. The box area for the SVM model is the largest among the four models, indicating the poorest performance. The box area for the BP model falls between those of the GPR and DT models, indicating a moderate performance. Both the GPR and DT models have smaller box areas; however, the GPR model has fewer discrete points. This suggests that among the four models, the GPR model exhibits the best performance. To verify whether the models were overfitting, a validation set was used to assess their performance. Because the dataset was sufficiently large, randomly selecting 350 data points for the validation set did not affect the conclusions. The error results of the four machine-learning models on the validation set are shown in Fig. 3d. We used the root-mean-square error as a performance metric for the machine-learning model, which amplified the performance differences of the model under large errors. The mean absolute error was also used to assess the average prediction accuracy of the model. Among the four models, the SVM model exhibited the largest differences in the residual values, indicating the worst generalization ability. However, the GPR model exhibited a smoother trend and the smallest differences in residual values, indicating the best generalization ability. The results of the residual plot were consistent with those of the box plot, indicating that overfitting did not occur and the model performance was reliable. Therefore, subsequent research used the GPR model to improve the positioning accuracy.

2.4.2 Position resolution under the GPR algorithm

This section presents the validation of the effectiveness of the simulation results by comparing the reconstructed muon-hit position images obtained in the experiments with those generated in the simulations. In the experiment, approximately 4×10^4 valid muon events were obtained through data selection and then divided into training, validation, and test sets in a $2 : 1 : 1$ ratio. The collected trigger time, time over threshold, and values obtained through the time-difference algorithms were used as the feature library for the GPR algorithm. In the simulation, the corresponding time information obtained through the Geant4 simulation served as the feature library for the GPR algorithm with an equal collection of 4×10^4 valid events. The reconstructed position results are presented in Fig. 4. The distribution of the reconstructed muon positions for the MWDC is shown in Fig. 4a, exhibiting a trend of more muons at the center and fewer muons at the edges. This is attributed to the pronounced edge effects of the outermost wires in the MWDC, which resulted in a lower count of valid muon data near the edges after selection. The project also compared the muon reconstruction effects of plastic scintillators with three- and four-corner PMT readouts, as depicted in the third image in Fig. 4a and the first image in Fig. 4b. The results indicate that using a three-corner PMT leads to a significant reduction in the accuracy of position reconstruction at the corner because of missing data from the PMT readout of the corner, causing a noticeable inward shift of the reconstructed points in that region. The position reconstruction results for plastic scintillators with four-corner PMT readouts are shown in Fig. 4b, where the lower data volume near the edges caused by the edge effects of the MWDC detector led to a training imbalance in the feature values. Consequently, the reconstruction results at the edges of the detector were inferior to those in the central region. The reconstructed position results from the simulations are shown in Fig. 4c. The results exhibit a more even distribution of data on the detector panel, resulting in better position reconstruction overall. However, the reconstruction results at the edge positions tended to deviate from the actual edges and shifted towards the interior. From Sect. 2, we can infer that we have calculated the critical angle for the total internal reflection on the surface of the PMT to be approximately 68.5°. Thus, in this situation, if the muon impact point is located at the edge of the detector, the scintillation light travels the shortest path to reach the two adjacent PMTs, exceeding the acceptance angle of the PMT photocathode. However, the scintillation light that reaches the PMT via a longer path owing to refraction remains unaffected. This results in a delay in the arrival time of the collected scintillation photons at these PMTs compared with the actual time. However, the propagation of the scintillation light to distant nonadjacent PMTs was not affected by this phenomenon. Therefore, the reconstructed image tended to bend inward at the edge positions.

The experiment yielded an average error of $\sigma_x = 20.9$ mm on the x-axis, $\sigma_y = 18.6$ mm on the y-axis, and an overall error of $\sigma = 27.9$ mm. In the 800 mm $\times$ 800 mm position reconstruction simulation, the average error on the x-axis was $\sigma_x = 9.6$ mm, that on the y-axis was $\sigma_y = 10.9$ mm, and the position resolution was $\sigma = 14.5$ mm.

2.4.3 Muon-track reconstruction

To investigate the effectiveness of the reconstruction of the muon trajectories in the detector system, as shown in Fig. 5a, when the distance between the detector panels changes, the corresponding angles vary, where $\theta_{1\max} < \theta_{2\max}$. Therefore, we simulated the reconstruction results for 100 muon trajectories to determine the effective angular resolution of the detector in this configuration. The angular distributions of the reconstructed trajectories are presented in Fig. 5b.

The muon flux at sea level followed a $\cos^2 \theta$ distribution relative to the zenith angle. Considering the detector-acceptance angles, the detected muon flux relative to the zenith angle

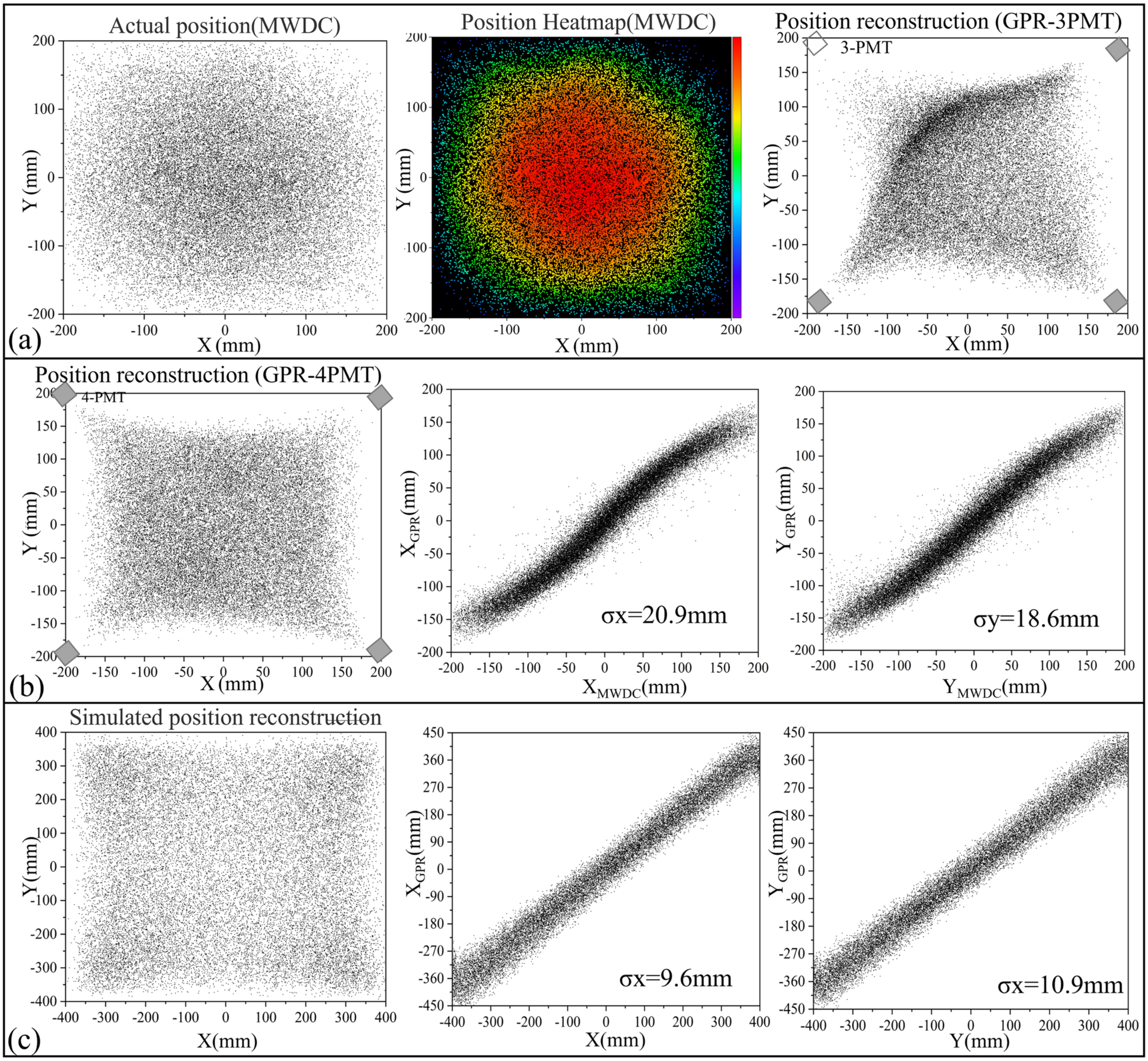

Fig. 4 (Color online) Comparison of experimental and simulated results. (**a**) Muon distribution measured by MWDC with muon-hit-position reconstruction under the three-corner readout for a 400 mm × 400 mm effective area. (**b**) Muon-hit-position reconstruction and position resolution obtained under the GPR algorithm for a 400 mm × 400 mm effective area. (**c**) Position reconstruction and position resolution under simulation

exhibited a distribution of $2\pi I_0 \int I(\theta) \sin\theta d\theta$. A comparison of this result with Fig. 5b shows that, despite some trajectory deviations due to precision errors, the overall distribution of muons aligned with the expected pattern within the detector structure.

3 Imaging results

3.1 Application of PoCA algorithm to scattering imaging

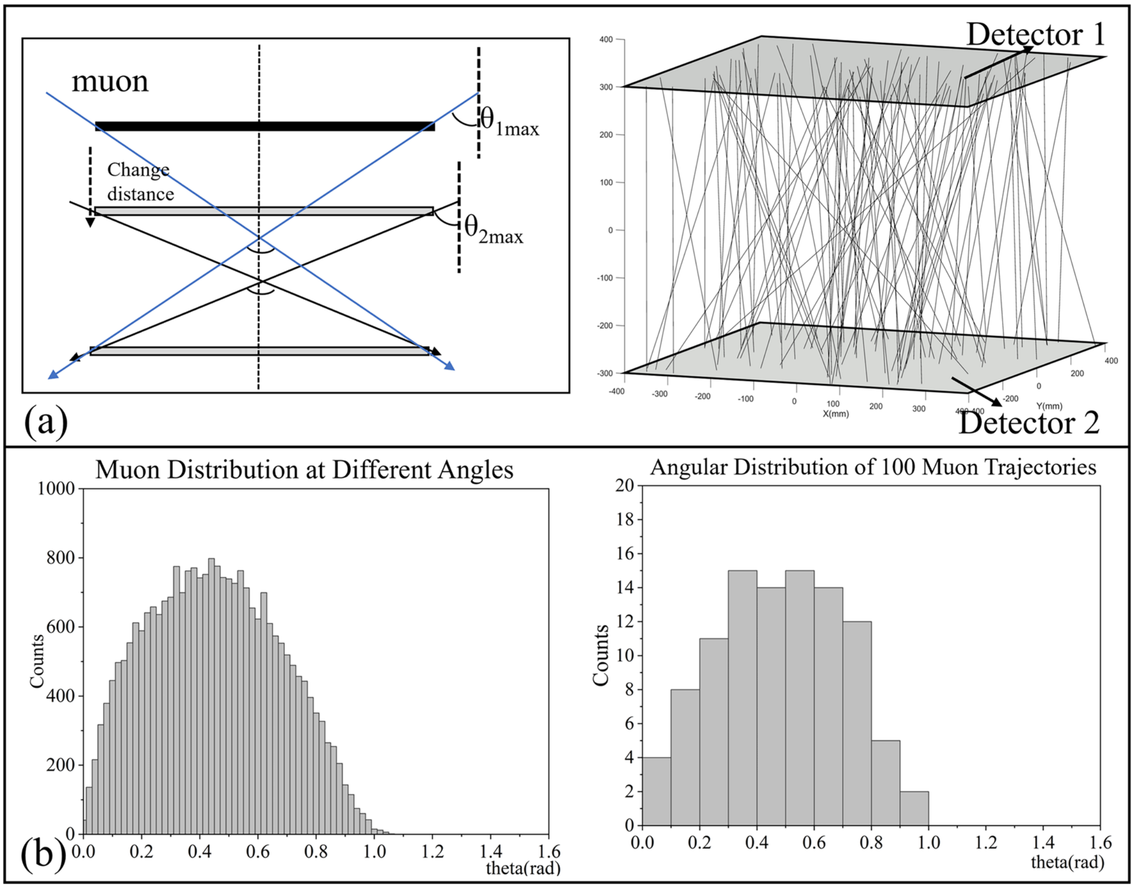

Fig. 5 (Color online) (**a**) Muon-track reconstruction. (**b**) Detector receivable angle

In the Point of Closest Approach (PoCA) algorithm, the multiple Coulomb scatterings of muons passing through the detection material are treated as individual scattering events. The muons passing through the detection region can be considered to occur at a single point. The muon-imaging algorithm is implemented based on an imaging framework similar to a grid search. In this framework, the detection region is divided into small rectangular boxes, called voxels. Each voxel is treated as the smallest unit of investigation for the Coulomb scattering. In n-dimensional space, the intersection of the incoming and outgoing lines of the muon is considered as the scattering point, where Coulomb scattering occurs. In 3D space, the incident and exit lines are generally not coplanar; therefore, the scattering point is taken as the midpoint of the perpendicular line connecting the incident and exit lines. Using the muon entrance and exit lines and the scattering point, the trajectory of the muon and the voxels it passes through may be determined.

3.2 Scattering imaging results for simple models

To validate the imaging capabilities of the detector system, an imaging model was constructed, as shown in Fig. 6. The target object consists of tungsten blocks arranged to form the letters "u," "s," and "c" with the red box representing the actual dimensions of the objects. The reconstructed image area was 800 mm $\times$ 800 mm and the individual pixel block area was 4 mm $\times$ 4 mm. The incident muon count was 6×10^7, which is equivalent to an actual imaging time of approximately four days, based on the natural muon flux. The imaging results indicate that the system can achieve shape differentiation for large high-atomic-number objects. However, the boundary positions of the imaged objects appeared somewhat blurred; thus, distinguishing the boundaries of the tungsten blocks was challenging. However, the approximate shapes of the tungsten blocks could be discerned using a heatmap. Therefore, this system is suitable for scatter imaging and can be used to image large objects.

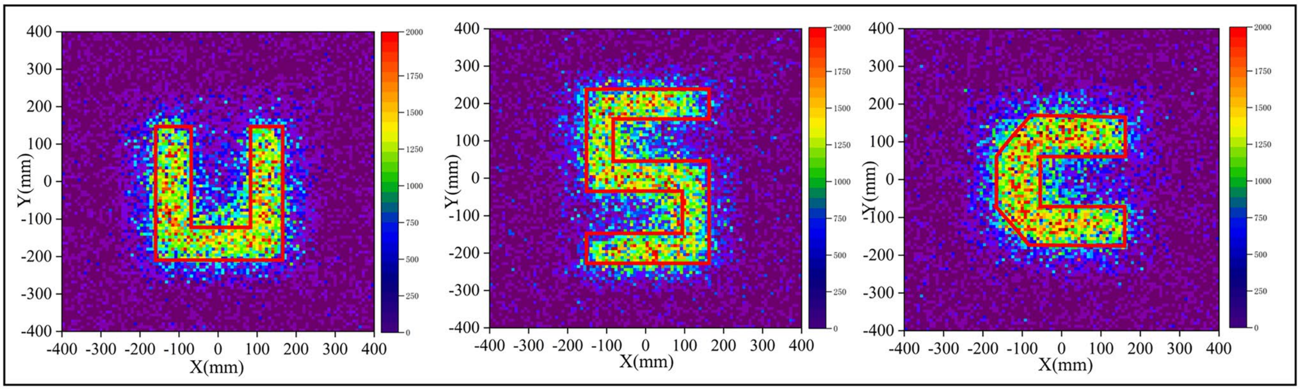

Fig. 6 (Color online) Imaging of large objects of different shapes

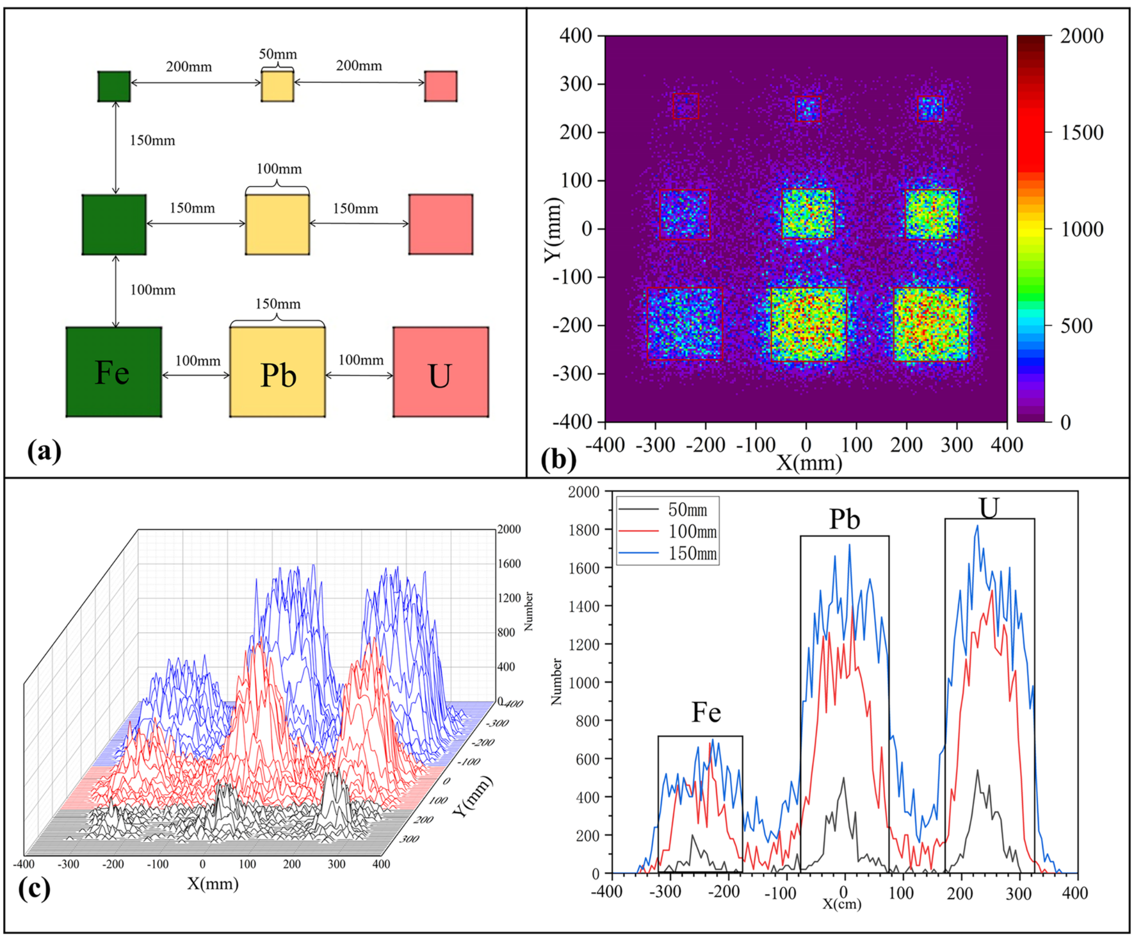

Fig. 7 (Color online) (**a**) Schematic of the imaging model. (**b**) Top view of PoCA scattering chromatography imaging. (**c**) Three-dimensional plot and front view of the trend of the number of PoCA points with the position

3.3 Results for complex model

To verify the imaging performance in complex environments and expand the scope of applications, a complex model was constructed, as shown in Fig. 7a. The model comprised nine blocks, including three sets of uranium, lead, and iron blocks of different sizes (side lengths of 50, 100, and 150 mm). The distances between blocks with side lengths of 150, 100, and 50 mm were 100, 150, and 200 mm, respectively.

The imaging results of the complex model are shown in Fig. 7b, where the red wire frames represent the actual object sizes. From the top view, numerous noise points can be observed along the boundary positions of the object blocks, resulting in shape deformation. The distance between blocks with a side length of 150 mm was indistinguishable. The distance between the three blocks with a side length of 100 mm was discernible, but the boundaries appeared blurred. Low-*Z* iron with a side length of 50 mm could not be effectively imaged. To verify the reconstruction accuracy of the method, a 3D trend map was constructed using the slice method, as shown in the left panel of Fig. 7c. The high-*Z* material object was effectively discriminated at all three distances and exhibited no mixing. However, for low-*Z* iron, when the distance between the object block models was 100 mm, no clear transition was observed between the edge counts of the iron block model and the noise points; thus, distinguishing the boundary of the iron model was difficult. The trend-change graph of the center position for the three sets of objects of different sizes is shown in the right panel of Fig. 7c. The results suggest a subtle difference among high-*Z* materials such as lead and uranium. While a more pronounced distinction is observed between high- and low-*Z* materials, the system cannot differentiate between specific types of high-*Z* materials. Steep rising and falling edges were used as criteria to distinguish the boundaries of the models. For objects with a side length of 150 mm, the imaging size was approximately 200 mm, resulting in an imaging-resolution error of 50 mm. For objects with a side length of 100 mm, the imaging resolution was lower.

4 Conclusion

In this study, we successfully developed and tested a plastic scintillator muon detector using machine-learning algorithms. Conducting experiments at the Institute of Modern Physics in Lanzhou, we performed muon-position resolution tests using an MWDC. We evaluated the position-reconstruction performance of the detector by considering a limited detection area in the experimental setup. To showcase the reconstruction capabilities over a larger area, we expanded the detection area to 800 mm × 800 mm in the simulations, while maintaining consistent structural and performance parameters for a reliable comparison with the experimental results. We selected the GPR algorithm for position reconstruction and incorporated the TDOA algorithm as a feature in the GPR model. In the simulation, large-area plastic scintillator detectors achieved a position resolution better than 2 cm. In the experimental platform tests, the position resolution of the test detectors was 27.9 mm. In the analysis of the position resolution, we considered factors such as the critical angle for total internal reflection in the PMT and the distribution pattern of muons on the MWDC. Both influence the algorithm model and ultimately affect the resolution. Through simulations of the imaging of large objects and materials with different atomic numbers, we demonstrated the capability of the system to image high- and low-*Z* materials in the constructed model, accurately distinguishing materials with significant density differences. The image reconstruction of high-*Z* materials with dimensions of 150, 100, and 50 mm achieved a precision of 50 mm, satisfying the requirements for rapid imaging. However, differentiating between high-*Z* materials is challenging.

Despite the lower imaging accuracy compared with gas detectors such as MWDC or MRPC, our detector system exhibited inherent advantages in terms of portability, lightweight design, and cost-effectiveness. To leverage these advantages, we plan to deploy our detector system for imaging large geological objects, such as mines and caves, where stringent precision requirements are not essential.

Acknowledgements I am deeply grateful to Professor Yu-Hong Yu at the Institute of Modern Physics, China, for providing the essential detector testing platform that significantly supported our experiments. Special thanks to Dr. Xiang-Man Liu and Mr. Jie-Lei Zhang for their invaluable guidance and patient assistance during the experimental process. Their expertise was instrumental to the success of this study.

Author contributions All authors contributed to the study conception and design. Material preparation and data collection were performed by Xiang-Man Liu, Hai-Feng Zhang, Wan-Cheng Xiao, Yu-Cheng Zou, and Yu-He Huang. Data analysis and computation were performed by Lie He and Si-Yuan Luo. The first draft of the manuscript was written by Lie He, and manuscript revisions were completed by Si-Yuan Luo and Xiao-Dong Wang. All authors commented on previous versions of the manuscript. All authors read and approved the final manuscript.

Data availability The data that support the findings of this study are openly available in Science Data Bank at https://cstr.cn/31253.11.sciencedb.j00186.00194 and https://www.doi.org/10.57760/sciencedb.j00186.00194.

Declarations

Conflict of interest The authors declare that they have no conflict of interest.

References

1. S.H. Neddermeyer, C.D. Anderson, Cosmic-ray particles of intermediate mass. Phys. Rev. **54**, 88 (1938). https://doi.org/10.1103/PhysRev.54.88.2
2. M. Tanabashi, P.D. Grp, K. Hagiwara et al., Review of particle physics: particle data group. Phys. Rev. D. **98**, 030001 (2018). https://doi.org/10.1103/PhysRevD.98.030001
3. T.D. Lee, H. Robinson, M. Schwartz et al., Intensity of upward muon flux due to cosmic-ray neutrinos produced in the atmosphere. Phys. Rev. **132**, 1297–1300 (1963). https://doi.org/10.1103/physrev.132.1297

4. S.H. Neddermeyer, C.D. Anderson, Note on the nature of cosmic-ray particles. Phys. Rev. **51**, 884–886 (1937). https://doi.org/10.1103/physrev.51.884
5. N. Lesparre, D. Gibert, J. Marteau et al., Geophysical muon imaging: feasibility and limits. Geophys. J. Int. **183**, 1348–1361 (2010). https://doi.org/10.1111/j.1365-246X.2010.04790.x
6. D. Schouten, P. Ledru, Muon tomography applied to a dense uranium deposit at the McArthur river mine. J. Geophys. Res. Solid Earth. **123**, 8637–8652 (2018). https://doi.org/10.1029/2018JB015626
7. G. Saracino, L. Amato, F. Ambrosino et al., Imaging of underground cavities with cosmic-ray muons from observations at Mt Echia (Naples). Sci Rep. **7**, 1181 (2017). https://doi.org/10.1038/s41598-017-01277-3
8. L.W. Alvarez, J.A. Anderson, F.E. Bedwei et al., Search for hidden chambers in the pyramids. Science **167**, 3919 (1970). https://doi.org/10.1126/science.167.3919.832
9. G. Leone, H.K.M. Tanaka, M. Holma et al., Muography as a new complementary tool in monitoring volcanic hazard: implications for early warning systems. Proc. R. Soc. A. **477**, 2255 (2021). https://doi.org/10.1098/rspa.2021.0320
10. R. Han, Q. Yu, Z. Li et al., Cosmic muon flux measurement and tunnel overburden structure imaging. JINST. **15**, 06019 (2020). https://doi.org/10.1088/1748-0221/15/06/P06019
11. R. Nishiyama, A. Ariga, T. Ariga et al., First measurement of ice-bedrock interface of alpine glaciers by cosmic muon radiography. Geophys. Res. Lett. **44**, 12 (2017). https://doi.org/10.1002/2017GL073599
12. K. Morishima, M. Kuno, A. Nishio et al., Discovery of a big void in Khufu's Pyramid by observation of cosmic-ray muons. Nature **552**, 386–390 (2017). https://doi.org/10.1038/nature24647
13. S. Xiao, W.B. He, M.C. Lan et al., A modified multi-group model of angular and momentum distribution of cosmic ray muons for thickness measurement and material discrimination of slabs. Nucl. Sci. Tech. **29**, 28 (2018). https://doi.org/10.1007/s41365-018-0363-7
14. S. Barnes, A. Georgadze, A. Giammanco et al., Cosmic-ray tomography for border security. Instruments **7**, 13 (2023). https://doi.org/10.3390/instruments7010013
15. X.Y. Pan, Y.F. Zheng, Z. Zeng et al., Experimental validation of material discrimination ability of muon scattering tomography at the TUMUTY facility. Nucl. Sci. Tech. **30**, 120 (2019). https://doi.org/10.1007/s41365-019-0649-4
16. L.X. Chen, L. Zhang, G.Y. Wang et al., Imaging multi-materials tightly combined objects by applying grey relational analysis in muon tomography. Prog. Nucl. Energ. **154**, 104416 (2022). https://doi.org/10.1016/j.pnucene.2022.104416
17. I. Bikit, D. Mrdja, K. Bikit et al., Novel approach to imaging by cosmic-ray muons. EPL **113**, 58001 (2016). https://doi.org/10.1209/0295-5075/113/58001
18. G. Galgoczi, D. Mrdja, I. Bikit et al., Imaging by muons and their induced secondary particles-a novel technique. J. Instrum. **15**, 06014 (2020). https://doi.org/10.1088/1748-0221/15/06/C06014
19. S.Y. Luo, Y.H. Huang, X.T. Ji et al., Hybrid model for muon tomography and quantitative analysis of image quality. Nucl. Sci. Tech. **33**, 81 (2022). https://doi.org/10.1007/s41365-022-01070-6
20. X.T. Ji, S.Y. Luo, Y.H. Huang et al., A novel 4D resolution imaging method for low and medium atomic number objects at the centimeter scale by coincidence detection technique of cosmic-ray muon and its secondary particles. Nucl. Sci. Tech. **33**, 2 (2022). https://doi.org/10.1007/s41365-022-00989-0
21. M. Bramer, Volumes of human learning on machine learning. Nature **337**, 315 (1989). https://doi.org/10.1038/337315a0
22. P.D. Luna, J. Wei, Y. Bengio et al., Use machine learning to find energy materials. Nature **552**, 23–27 (2017). https://doi.org/10.1038/d41586-017-07820-6
23. K. Aktas, M. Kiisk, A. Giammanco et al., A comparison of neural networks and center of gravity in muon hit position estimation. Entropy **24**, 1659 (2022). https://doi.org/10.3390/e24111659
24. W.B. He, Dissertation, Nuclear Science and Technology University of Science and Technology of China, 2019 (in Chinese)
25. G. Baccani, L. Bonechi, D. Borselli et al., The MIMA project Design, construction and performances of a compact hodoscope for muon radiography applications in the context of archaeology and geophysical prospections. JINST. **13**, 11001 (2018). https://doi.org/10.1088/1748-0221/13/11/P11001
26. B.X. Qi, S.B. Liu, H. Ji et al., A novel method of encoded multiplexing readout for micro-pattern gas detectors. Chin. Phys. C **40**, 056102 (2016). https://doi.org/10.1088/1674-1137/40/5/056102
27. Y. Wang, Z.Y. Zhang, S.B. Liu et al., A high spatial resolution muon tomography prototype system based on micromegas detector. IEEE. T. NUCL. SCI. **69**, 78–85 (2022). https://doi.org/10.1109/TNS.2021.3137415
28. J.B. Xi, H. Liang, S.T. Xiang et al., Upgrade to the front-end electronics of the BESIII muon identification system. Nucl. Sci. Tech. **25**, 020402 (2014). https://doi.org/10.13538/j.1001-8042/nst.25.020402
29. S. Harada, T. Nishigaki, N. Kitagawa et al., Development of high-resolution nuclear emulsion plates for synchrotron X-ray topography observation of large-size semiconductor wafers. J. Electron. Mater. **52**, 2951–2956 (2023). https://doi.org/10.1007/s11664-023-10270-8
30. H. Yang, G. Lou, T. Yu et al., MuGrid: a scintillator detector towards cosmic muon absorption imaging. Nucl. Instru. Meth. A **1042**, 167402 (2022). https://doi.org/10.1016/j.nima.2022.167402
31. M. Li, Z.M. Wang, C.M. Liu et al., Performance of compact plastic scintillator strips with wavelength shifting fibers using a photomultiplier tube or silicon photomultiplier readout. Nucl. Sci. Tech. **34**, 31 (2023). https://doi.org/10.1007/s41365-023-01175-6
32. K.Q. Yao, Z.D. Li, Z.Y. Liu et al., Concept design and feasibility study of novel calorimeter-type borehole muon detector. Nucl. Instru. Meth. A **1049**, 168074 (2023). https://doi.org/10.1016/j.nima.2023.168074
33. S.W. Tang, Y.H. Yu, Y. Zhou et al., A large area plastic scintillation detector with 4-corner-readout. Chin. Phys. C **40**, 056001 (2016). https://doi.org/10.1088/1674-1137/40/5/056001
34. Eljen Technology. EJ-200 Plastic Scintillator Data Sheet, www.eljentechnology.com/products/plastic-scintillators/ej-200-ej-204-ej-208-ej-212; 2018(accessed 2 April 2018)
35. C. Hagmann, D. Lange, D. Wright, Cosmic-ray shower generator (CRY) for Monte Carlo transport codes. IEEE. Nucl. Sci. Symp. Conf. Rec. **2**, 1143–1146 (2007). https://doi.org/10.1109/NSSMIC.2007.4437209
36. R. Ogawara, M. Ishikawa, Signal pulse emulation for scintillation detectors using Geant4 Monte Carlo with light tracking simulation. Rev. Sci. Instrum. **87**, 075114 (2016). https://doi.org/10.1063/1.4959186
37. J. Nam, Y. Choi, D. Kim et al., A detailed Monte Carlo simulation for the Belle TOF system. Nucl. Instrum. Meth. A. **491**, 54 (2002). https://doi.org/10.1016/S0168-9002(02)01231-7
38. P. Ma, Dissertation, University of Chinese Academy in Nuclear Technology and Application, 2019 (in Chinese)
39. B. Xu, G. Sun, R. Yu et al., High-accuracy TDOA-based localization without time synchronization. IEEE Trans. Parallel Distrib. Syst. **24**, 1567–1576 (2013). https://doi.org/10.1109/TPDS.2012.248